

## PHYSICS

# Orbital-selective Kondo lattice and enigmatic *f* electrons emerging from inside the antiferromagnetic phase of a heavy fermion

Ioannis Giannakis<sup>1</sup>, Justin Leshen<sup>1</sup>, Mariam Kavai<sup>1</sup>, Sheng Ran<sup>2,3\*</sup>, Chang-Jong Kang<sup>4</sup>, Shanta R. Saha<sup>2,3</sup>, Y. Zhao<sup>2,5</sup>, Z. Xu<sup>2\*</sup>, J. W. Lynn<sup>2</sup>, Lin Miao<sup>6,7</sup>, L. Andrew Wray<sup>6</sup>, Gabriel Kotliar<sup>4,8</sup>, Nicholas P. Butch<sup>2,3</sup>, Pegor Aynajian<sup>1†</sup>

Novel electronic phenomena frequently form in heavy-fermions because of the mutual localized and itinerant nature of *f*-electrons. On the magnetically ordered side of the heavy-fermion phase diagram, *f*-moments are expected to be localized and decoupled from the Fermi surface. It remains ambiguous whether Kondo lattice can develop inside the magnetically ordered phase. Using spectroscopic imaging with scanning tunneling microscope, complemented by neutron scattering, x-ray absorption spectroscopy, and dynamical mean field theory, we probe the electronic states in antiferromagnetic  $\text{USb}_2$ . We visualize a large gap in the antiferromagnetic phase within which Kondo hybridization develops below  $\sim 80$  K. Our calculations indicate the antiferromagnetism and Kondo lattice to reside predominantly on different *f*-orbitals, promoting orbital selectivity as a new conception into how these phenomena coexist in heavy-fermions. Finally, at 45 K, we find a novel first order-like transition through abrupt emergence of nontrivial 5*f*-electronic states that may resemble the “hidden-order” phase of  $\text{URu}_2\text{Si}_2$ .

## INTRODUCTION

The dual nature of the *f* electronic wave function in heavy fermions drives fascinating electronic behaviors, from exotic orders (1) to quantum criticality (2) and emergent superconductivity (3–5). The stage is set at relatively high temperatures by the local Kondo interaction of the *f* moments. As temperature is lowered below the so-called coherence temperature, hybridization of these *f* moments with conduction electrons drives the hitherto localized *f* electrons into the Fermi sea, enlarging the Fermi surface (6). Whether the Kondo quenching is complete depends on its competition with the Ruderman-Kittel-Kasuya-Yosida (RKKY) interaction that tends to stabilize long-range magnetic order. Theoretically, two scenarios regarding the zero temperature phase diagram of heavy fermions, have been put forward. The first describes the phase diagram with two separate quantum critical points (QCPs), one for the onset of long-range magnetic order and another for the destruction of the Kondo lattice. In the second scenario, both phenomena vanish simultaneously at a single QCP (7–11). Over the past decade, theoretical and experimental efforts have focused on this very matter of understanding which scenario better describes the phase diagram of the different heavy fermion material systems. There may now be consensus that, at least,  $\text{YbRh}_2\text{Si}_2$  follows the latter scenario of the Kondo destruction at the magnetic QCP (12, 13). Yet, a comprehensive picture remains missing. Differentiating these scenarios not only provides an understanding of the complex phase diagram

of heavy fermions but also describes the nature of the unconventional critical fluctuations that occur on an extended phase space near the QCP (the quantum critical fan), out of which unconventional superconductivity often emerges.

In 4*f* electron systems, such as Ce- and Yb-based heavy fermions (typically with a valence close to 4*f*<sup>1</sup> and 4*f*<sup>13</sup> leading to one *f* electron and one *f* hole, respectively), the *f* orbitals are relatively localized at high temperature, and the low-temperature properties are well described by the Kondo lattice model. On the other hand, in 5*f* electron systems, such as U-based heavy fermions (where determining the valence, typically ranging between 5*f*<sup>1</sup> and 5*f*<sup>3</sup>, is more challenging), the spatial extent of the 5*f* orbitals and their hybridization with ligand orbitals (conduction electrons) give the *f* electrons an intermediate character between partial itineracy and partial localization, increasing the complexity of the Kondo lattice problem. U-based heavy fermion systems therefore provide an ideal platform to probe this rich and complex physics.

$\text{USb}_2$  features one of the highest antiferromagnetic (AFM) transition temperatures ( $T_N$ ) in *f* electron systems with  $T_N$  exceeding 200 K (14). Angle-resolved photoemission spectroscopy (ARPES) (15) and de Haas-van Alphen (dHvA) (16) experiments indicate two-dimensional cylindrical Fermi surface sheets in the AFM phase. Resistivity measurements (17) along the *c* axis reveal a peak around 80 K, which may resemble a Kondo coherence-like behavior well below  $T_N$ , yet its true origin remains unknown. Despite the high AFM transition temperature, specific heat (16) indicates a sizable Sommerfeld coefficient of 27 mJ/mol·K<sup>2</sup>, further providing indications of low-temperature itinerant heavy quasiparticles residing near the Fermi energy ( $E_F$ ). Spectroscopic investigation of  $\text{USb}_2$ , a clean stoichiometric metal with a very large  $T_N$ , may therefore provide invaluable information on the interplay between magnetic ordering and Kondo breakdown phenomena. Moreover, the robust AFM in  $\text{USb}_2$ , which drives out of strong correlations, has become particularly interesting very recently as it has been shown that it can be tuned toward quantum critical and tricritical points (18, 19), opening new avenues for emerging phenomena.

Copyright © 2019  
The Authors, some  
rights reserved;  
exclusive licensee  
American Association  
for the Advancement  
of Science. No claim to  
original U.S. Government  
Works. Distributed  
under a Creative  
Commons Attribution  
NonCommercial  
License 4.0 (CC BY-NC).

<sup>1</sup>Department of Physics, Applied Physics, and Astronomy, Binghamton University, Binghamton, NY 13902, USA. <sup>2</sup>NIST Center for Neutron Research, National Institute of Standards and Technology, Gaithersburg, MD 20899, USA. <sup>3</sup>Center for Nanophysics and Advanced Materials, Department of Physics, University of Maryland, College Park, MD 20742, USA. <sup>4</sup>Department of Physics and Astronomy, Rutgers University, NJ 08854, USA. <sup>5</sup>Department of Materials Science and Engineering, University of Maryland, College Park, MD 20742, USA. <sup>6</sup>Department of Physics, New York University, New York, NY 10003, USA. <sup>7</sup>Advanced Light Source, Lawrence Berkeley National Laboratory, Berkeley, CA 94720, USA. <sup>8</sup>Condensed Matter Physics and Materials Science Department, Brookhaven National Laboratory, Upton, NY 11973, USA.

\*Present address: Department of Materials Science and Engineering, University of Maryland, College Park, MD 20742, USA.

†Corresponding author. Email: aynajian@binghamton.edu

Over the past several years, scanning tunneling microscopy (STM) experiments had considerable success in the imaging of heavy fermions and their formation (20–24), their transition into hidden order (20, 21, 25), and into heavy electron superconductivity (26, 27) in U-, Ce-, and Yb-based systems. However, in all these studied cases, the magnetically ordered phase and the impact of magnetism on heavy fermion and Kondo lattice formation have not been accessible. When the local *f* moments order into an AFM phase, can the Kondo lattice coherence still develop well below  $T_N$ , or does it simply break down? USb<sub>2</sub> is particularly selected to answer this question because of the large accessible temperature window below  $T_N$  within which the gradual evolution of the electronic states inside the AFM phase can be visualized.

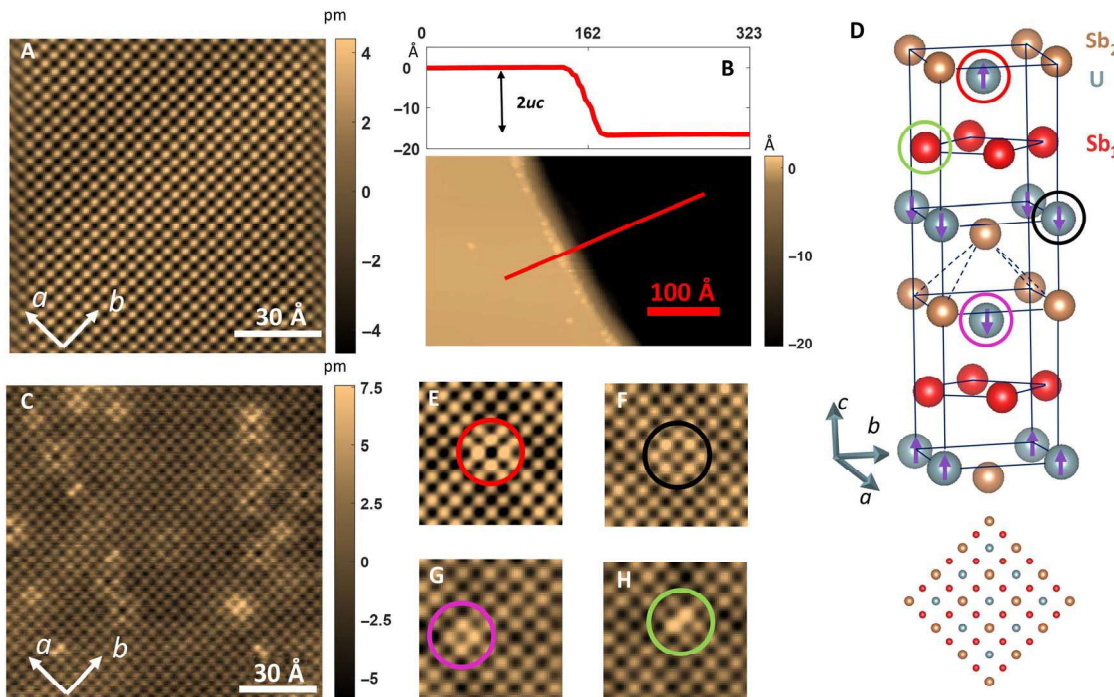
Using spectroscopic imaging with the STM complemented by elastic neutron scattering, we probe signatures of the magnetic order and the Kondo hybridization in USb<sub>2</sub> as a function of temperature. We find a large gap ( $\Delta = 60$  meV) in the tunneling density of states of USb<sub>2</sub>, which we associate to the AFM order, within which the Kondo hybridization near  $E_F$  develops with decreasing temperature. Its gradual onset near  $T = 80$  K coincides with the broad peak observed in resistivity measurements (16, 17). At low temperatures, we visualize the hybridization of this heavy band with the conduction electrons, together providing spectroscopically conclusive evidence of the Kondo coherence emerging from deep within the AFM phase. Our dynamical mean field theory (DMFT) calculations and spatial spectroscopic mapping provide a qualitative description of an orbital-selective

AFM order and the Kondo lattice that reside on different nondegenerate 5*f* orbitals, offering a new conception of how itinerant and localized *f* electrons can coexist in heavy fermions. Last, we found a novel first order-like electronic transition at  $T^* = 45$  K through the abrupt emergence of sharp *f* electronic states below ( $E_1 = -20$  meV) and above ( $E_2 = +30$  meV)  $E_F$  with distinct orbital character.

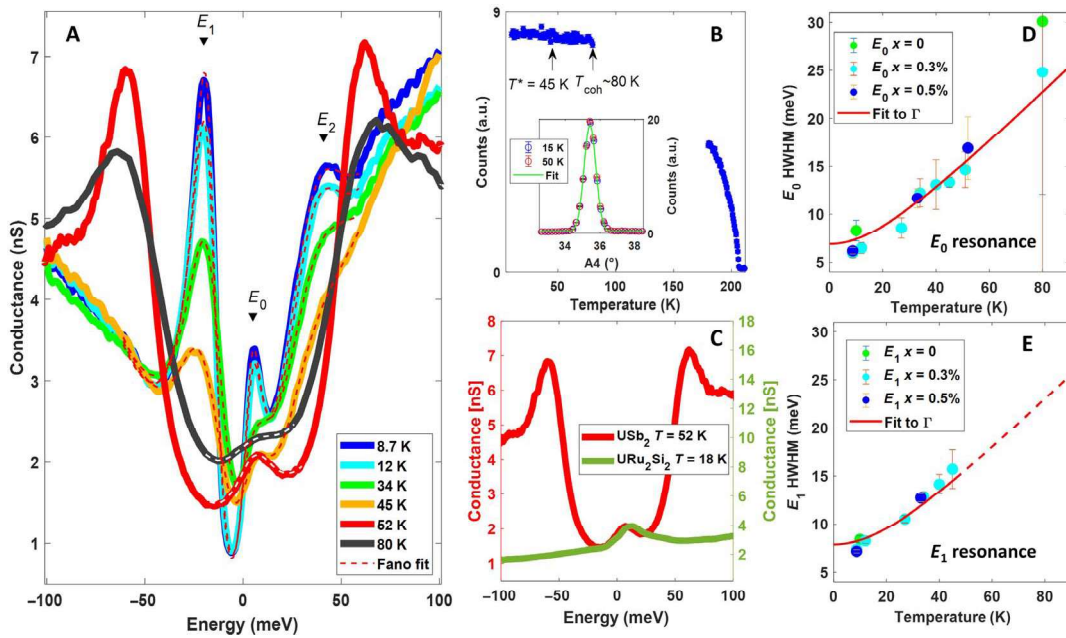
## RESULTS

Figure 1 (A and C) displays STM topographs of USb<sub>2</sub> and Th-doped U<sub>1-x</sub>Th<sub>x</sub>Sb<sub>2</sub> showing square atomic lattice with a spacing of 4.2 Å corresponding to the in-plane lattice constant of USb<sub>2</sub>. Occasionally, vertical terraces with spacing of multiples of 8.7 Å are observed that match the *c* axis of the USb<sub>2</sub> single crystal (Fig. 1B). At least six different single crystals (pure,  $x = 0.3\%$  Th doped and  $x = 0.5\%$  Th doped) were cleaved in the current study, and numerous areas (spanning several tens of micrometers) on each sample were probed with the STM. Only one kind of surface has been observed in all these trials, indicating that the cleaving occurs at the Sb<sub>2</sub> layer (see Fig. 1D) (28). Any other cleaving plane statistically results in two different exposed surfaces, not observed in the experiment (see fig. S1).

Figure 2A shows  $dI/dV$  spectra measured at various temperatures away from any defects or dopants on a 0.3% Th-doped U<sub>1-x</sub>Th<sub>x</sub>Sb<sub>2</sub>. The spectra away from defects are identical (within the experimental resolution) between all the different samples studied, independent of the minute Th doping (see fig. S2). At  $T = 80$  K, the spectrum shows a



**Fig. 1. Atomic structure of U<sub>1-x</sub>Th<sub>x</sub>Sb<sub>2</sub>.** (A) Constant current topographic image on USb<sub>2</sub>, taken at a set point bias of 500 mV and a current of 200 pA, showing the atomic surface. (B) The topograph shows two terraces separated by  $2x$  *c* axis exposing two surfaces with the same chemical termination. The panel above the topograph is a linecut, perpendicular to the step, crossing both terraces. (C) Constant current topographic image on the U<sub>1-x</sub>Th<sub>x</sub>Sb<sub>2</sub> for  $x = 0.5\%$ , taken at a set point bias of  $-400$  mV and a current of  $-1.5$  nA, showing the atomic surface with four distinct types of defects resulting from Th substitution of U atoms. (D) Crystal structure of USb<sub>2</sub>. The top layer corresponds to the Sb<sub>2</sub> layer exposed upon cleaving. The circles mark the position of Th substitutions across two unit cells. The lower panel is a top-down view of the top 3 layers (Sb<sub>2</sub>-U-Sb<sub>1</sub>). (E to H) Th substitutions of U atoms in the first (red circle), second (black circle), third (purple circle), and Sb<sub>1</sub> (green circle) layers, respectively. The colored circles show the location of the same defects in the compound's crystal structure (Fig. 1D).



**Fig. 2. Electronic states of  $\text{U}_{1-x}\text{Th}_x\text{Sb}_2$  and their temperature evolution.** (A) Evolution of the  $dI/dV$  spectra ( $V_{\text{bias}} = -400$  mV,  $I_{\text{set point}} = -2$  nA) from 80 to 8.7 K for  $x = 0.3\%$ . At  $T = 80$  K, a partial gap associated with the AFM state of  $\text{USb}_2$ , as well as a broad hump inside the AFM gap at  $E_0 = 5$  meV, can be seen. Below  $T^* = 45$  K, the spectral form changes abruptly, revealing two sharp peaks at  $E_1 = -20$  meV and  $E_2 = 30$  meV. The dashed lines are fit of the data to three Fano line shapes and a parabolic background. For the spectra above 50 K, only a single Fano is fitted. (B) Neutron scattering data of the temperature dependence of the AFM Bragg peak (1:1:0.5) that onsets at  $T_N = 203$  K. Inset: 0 – 20 of the magnetic Bragg peak at 10 K (blue dotted line) and a Gaussian fit (red line). a.u., arbitrary units. (C) STM spectra of  $\text{USb}_2$  and  $\text{URu}_2\text{Si}_2$  that show a similar structure near the Fermi energy. The  $\text{URu}_2\text{Si}_2$  spectrum is taken from (25). It corresponds to the Si-terminated surface, which is analogous to the  $\text{Sb}_2$ -terminated surface of  $\text{USb}_2$ . (D and E) Temperature dependence of the HWHM of the  $E_0$  and  $E_1$  resonances, respectively. The lines are fit to  $\Gamma = \sqrt{(\pi k_B T)^2 + 2(k_B T_K)^2}$ .

particle-hole symmetric partial gap in the local density of states via the suppression of spectral weight within  $\pm 60$  meV and its buildup in the coherence peaks right above. At this temperature,  $\text{USb}_2$  is deep in the AFM phase, and the observed spectral gap is therefore likely the result of the AFM order. To further elaborate, we carry out temperature-dependent elastic neutron scattering on the very same samples. Figure 2B shows the temperature dependence of the AFM (1:1:0.5) Bragg peak that onsets at  $T_N = 203$  K. The AFM ordering wave vector indicates a doubling of the Brillouin zone along the  $c$  axis (see Fig. 1D), folding of the band structure, and gapping over 60% of the Fermi surface at 80 K, as seen in our STM data (Fig. 2A). The multiorbital nature of the Fermi surface in  $\text{USb}_2$  makes it difficult to conclusively determine the origin of metallic AFM phase. However, from our neutron scattering data, we calculate a large magnetic moment of  $1.9 \mu_B/\text{U}$ , consistent with previous reports (14), indicating a rather local character.

Looking closer at the 80-K spectrum reveals a weak hump structure within the AFM gap around the energy  $E_0 \sim 5$  meV above  $E_F$  (Fig. 2A). As temperature is lowered to 52 K, the AFM gap deepens, the coherence peaks (above  $\pm 60$  meV) sharpen, and the hump at  $E_0$  gradually evolves into a pronounced peak-like structure. This resonance observed at  $E_0$  in  $\text{USb}_2$  is in analogy with a similar resonance observed in a different U-based heavy fermion, the celebrated  $\text{URu}_2\text{Si}_2$  (21, 25). Figure 2C compares STM spectra from the two material systems [ $\text{URu}_2\text{Si}_2$  spectra taken from (25)]. This unexpected similarity of the hump structure near the  $E_F$ , in rather two different materials, suggests a similar origin of the low-energy physics, which in  $\text{URu}_2\text{Si}_2$  has been attributed to heavy fermion formation above its hidden-order phase (20, 25). The energy position of the  $E_0$  resonance, which is related to the valence

of  $f$  electrons (6), being a few millielectron volts above  $E_F$  in both U systems, further indicates similar valence in both systems. This is in contrast to  $\text{CeCoIn}_5$  ( $4f^1$ ), where the resonance is located right at  $E_F$  (25). Yet, how a Kondo lattice develops well below a magnetically ordered phase in  $\text{USb}_2$  is a puzzle. To provide insights into this rather bizarre observation, we used DMFT to compute the temperature-dependent electronic structure of  $\text{USb}_2$ . We found predominantly a  $5f^2$  valence of the U electronic states, in good agreement with our x-ray absorption spectroscopy (see fig. S3). These calculations qualitatively predict both the AFM order and the Kondo behavior with orbital selectivity, where the  $m_j = \pm 5/2$  and  $\pm 3/2$  orbitals are responsible for the RKKY-type AFM order, while the  $m_j = \pm 1/2$  orbitals lead to the Kondo resonance near  $E_F$  (see fig. S4). Therefore, the different nondegenerate  $5f$  orbitals, which are separated in energy and likely in momentum space, display different characters where some are predominantly localized, giving rise to the AFM order, and some are Kondo screened, leading to itinerant quasiparticles. We refer to the latter as the orbital-selective Kondo effect.

Lowering the temperature further below  $T^* = 45$  K (a drop of only a few kelvin) reveals an abrupt change of the spectral structure in our STM experiments, signaling a sudden transition in the electronic density of states of  $\text{USb}_2$  (Fig. 2A). Note that thermal broadening, which can explain the sharpening of the spectra between 80 and 52 K, is far from describing the observed transition at 45 K. The most pronounced feature is the discontinuous formation of two sharp resonances at  $E_1 = -20$  meV and  $E_2 = +30$  meV, far below and above  $E_F$ . Possible artifacts arising from the STM tip junction as an explanation to the observed behavior can be excluded since the observed results

were reproduced on three different samples, using three different STM tips, and in both cases of crossing  $T^* = 45$  K from below (warming up) and above (cooling down) (see fig. S2). Such a drastic change of the spectral structure with temperature has not been seen in any of the Ce-, Yb-, or Sm-based heavy fermion systems studied so far by STM or ARPES. While the  $E_{1,2}$  resonances emerge abruptly, the resonance at  $E_0$ , closer to the  $E_F$ , continues to evolve rather gradually with decreasing temperature in analogy with signatures of the Kondo lattice formation observed in other heavy fermion systems.

The cotunneling mechanism from the STM tip to a sharp resonance in the sample's local density of states manifests itself in a Fano line shape (29–31). To extract their temperature evolution, we fit the spectra in Fig. 2A to three distinct Fano line shapes centered around  $E_{1,2}$  and  $E_0$  with a parabolic background (see fig. S5). The model is an excellent fit to the data shown as thin dashed lines on top of each spectrum (Fig. 2A). The extracted linewidths of the resonances at  $E_0$  and  $E_1$  are displayed in Fig. 2 (D and E) (see section S5). As seen in the raw data, the resonance at  $E_0$  gradually grows below  $\sim 80$  K, providing a long-awaited explanation to the broad peak observed in resistivity measurements. Note that the true thermal evolution of the  $E_0$  (also  $E_{1,2}$ ) peak is difficult to extract from the spectra because of the constant current set point effect of STM experiments. Similarly, the width of the resonance at  $E_0$  decreases in the same temperature range and saturates at low temperature to an intrinsic linewidth expressed in half width at half maximum (HWHM) of  $\Gamma = 6 \pm 2$  meV. We can analyze the temperature broadening of the linewidth using the Kondo impurity model  $\Gamma = \sqrt{(\pi k_B T)^2 + 2(k_B T_K)^2}$ , which previously has well captured the temperature dependence in the Kondo lattice systems (20, 24). A fit (of a single parameter) of the above equation to the data yields a temperature of  $T_K = 55 \pm 20$  K (see Fig. 2D and section S5), which is related to the intrinsic linewidth of the Kondo resonance at  $T = 0$  K. Because of the valence state, in U compounds the Kondo resonance appears a few millielectron volts above  $E_F$  (21, 25), whereas in Ce (26, 27), Sm (32–34), and Yb (24) compounds, it is observed to be right above at and right below  $E_F$ , respectively. The fact that  $E_0$  is in the unoccupied side of the  $E_F$  places ARPES experiments to probe the line shape of the resonance at a disadvantage.

In contrast to this  $E_0$  resonance, that at  $E_1$  (and  $E_2$ ) follows a very unconventional temperature dependence. Its abrupt onsets at  $T^* = 45$  K closely match with the sharp anomaly seen in specific heat and the sudden release of entropy [see Supplementary Materials in (35)]. Similarly, optical pump probe spectroscopy (35) also sees an abrupt change at  $T^* = 45$  K in the lifetime of spin excitations, indicating the opening of a new decay channel, whereas low-temperature ARPES (36) sees a flat band at the same energy and widths as our  $E_1$  resonance. The energy separation between the two resonance levels of  $\delta_{1-2} = 50$  meV seen in our spectroscopic measurements corresponds to an excitation temperature exceeding 500 K. Neither their onset nor their signature in specific heat can be explained by the thermal population of conventional crystal electric field levels and Schottky anomaly. Together, these observations hint to an electronic transition in the bulk. Its energy being far from  $E_F$  ( $E_1 \gg k_B T$ ) also makes it less sensitive to measurements such as resistivity, and only the tail of the  $E_1$  resonance near  $E_F$  will be captured by transport studies. Once again, our DMFT calculations provide an insight into the origin of these  $f$  electronic states. As temperature is lowered, DMFT indicates two peaks that form around  $\pm 30$  meV of predominantly  $m_f = \pm 3/2$  orbital character, qualitatively in agreement with our observation. While neither their sharpness nor their

sudden onset is captured by these calculations, their distinct orbital character, nevertheless, suggests that some forms of orbital ordering may be behind the experimentally observed transition.

To gain access to the origin and the energy-momentum structure of these sharp resonances at  $E_{1,2}$  and  $E_0$ , we carry out spectroscopic imaging with the STM (37) at  $T = 8.7$  K. To enhance the scattering signal on a rather clean system (see Fig. 1A), we introduce Th substitution in  $U_{1-x}Th_xSb_2$ . STM topographs, shown in Fig. 1C, reveal four sets of defects, three of which correspond to the Th atoms replacing the U atoms in three consecutive U layers (Fig. 1, E to G) and one of which corresponds to the Th atoms replacing  $Sb_1$  (Fig. 1H) (see fig. S1). At these low concentrations ( $x = 0.3$  and 0.5%), the thermodynamic properties of  $USb_2$  are unchanged. We first look spatially at isolated Th dopants with atomic resolution (Fig. 3A). The local tunneling density of states measured on a (nonmagnetic) Th atom that substitutes a (magnetic) U atom right below the surface contrasted with one measured on a clean area away from dopants is shown in Fig. 3B (high temperature) and Fig. 3C (low temperature). At both temperatures, the spectral features associated with the AFM gap and sharp resonances all exhibit notable suppression near the Th atoms (Fig. 3, B and C), indicating that they originate from electronic states with  $f$  character. The Th atoms in this case are well represented by the so-called Kondo hole picture. In recent years, extensive theoretical work (38–40) has been carried out on modeling the electronic states surrounding a Kondo hole. The predicted impact of these Kondo holes is the atomic scale oscillations of the hybridization strength (38–41). The experimental linewidth  $\Gamma$  of the Kondo resonance at  $E_0$  is a measure of the Kondo hybridization strength (see section S6). From subatomic resolution spectroscopic imaging maps near the Th atoms, we extract the spatial variation of the resonance linewidth, energy, and asymmetry  $q$  parameter at low temperature (see fig. S6). The results are displayed in Fig. 3 (D to I). The first notable observation is the spatial extent of the hybridization (particularly that at  $E_0$ ) spanning a surface area of  $\sim 50$  to 100 U-sites. The size of this local perturbation is similar to what has been observed around Kondo holes in  $URu_2Si_2$  (41) and also comparable to the local hybridization seen around single Kondo impurities in metals (42). The second observation is oscillatory patterns forming spatially anisotropic ripple-like structures around the Th dopants, theoretically predicted to form near the Kondo holes (see fig. S7) (38, 39). Note that, theoretically, the oscillation in energy and the  $q$  parameter have not been considered. However, since the  $q$  parameter represents the relative tunneling to the resonant states at  $E_0$ , oscillation in the hybridization strength is therefore expected to drive a similar oscillatory behavior in the  $q$  parameter (see section S6). Last, the different magnitudes of the  $q$  parameter [sensitivity of tunneling to different orbitals (22)] for the  $E_0$ ,  $E_1$ , and  $E_2$  resonances, as well as their different spatial dependence (refer to section S6 and fig. S7), suggest that different nondegenerate  $f$  orbitals are responsible for the different resonances, supporting the mechanism of orbital selectivity proposed by our DMFT calculations.

We now move to probe the quasiparticle interference (QPI) off Th dopants. Elastic scattering and interference of quasiparticles from impurities give rise to standing waves in the constant energy conductance maps at wavelengths corresponding to  $2\pi/q$ , where  $q = k_f - k_i$  is the momentum transfer between initial ( $k_i$ ) and final ( $k_f$ ) states at the same energy. Note that the oscillatory behavior of the resonance linewidth discussed above is different from the QPI at a constant energy. Figure 4 (A to E) shows large-scale (50 nm) conductance maps at selected energies showing QPI near the Th atoms. The Fourier transform (FT)

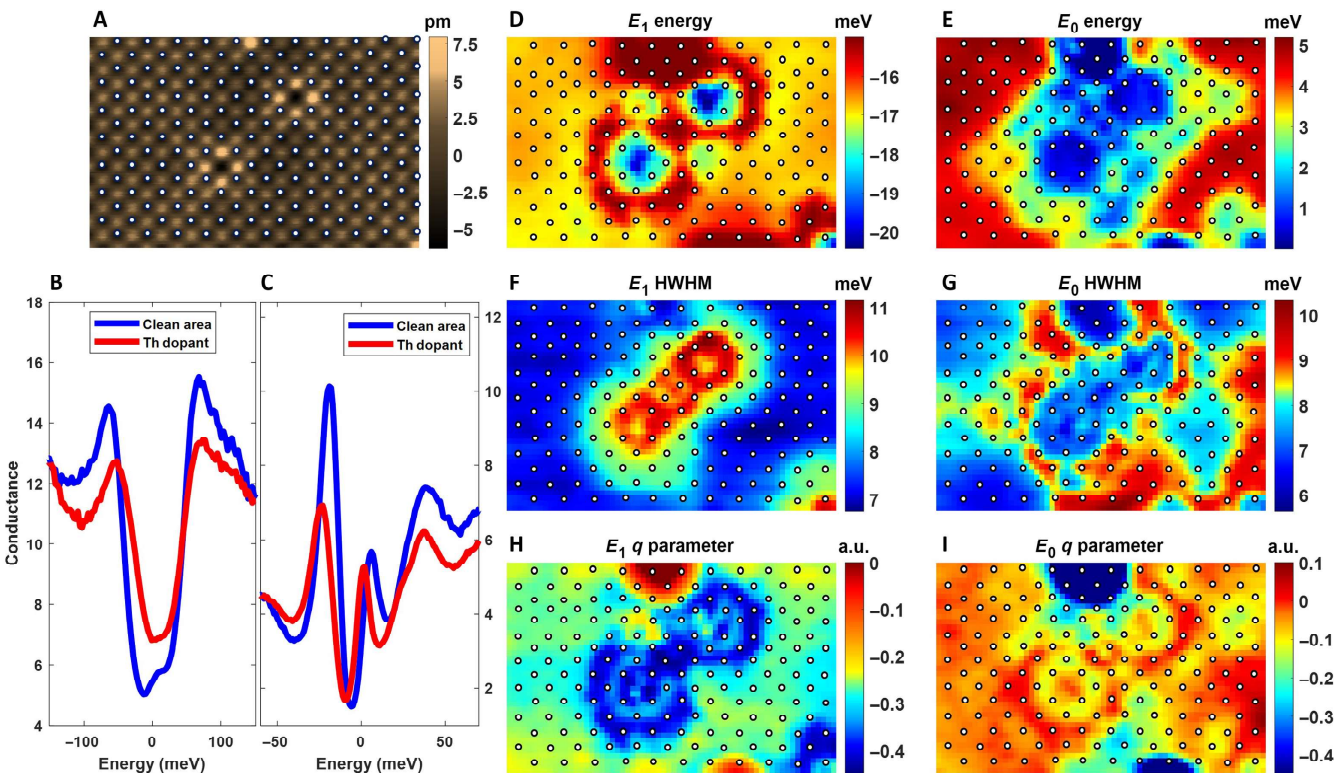


**Fig. 3. Spectroscopic imaging of the Kondo holes.** (A) Topographic image showing two Th dopants and a dimer defect on the top center of the image. (B and C)  $dI/dV$  spectra taken on a clean area (blue) and on a Th dopant (red) at 80 and 12 K, respectively. The spectral features related to the AFM gap and the sharp resonances are suppressed near the Th dopant. Conductance is given in nS. (D to I) Spatial modulation in the vicinity of the Th dopants of the hybridization energies (D and E), the linewidth (F and G), and  $q$  parameter (H and I) for the peaks at  $E_1$  and  $E_0$  extracted from fits to the Fano line shape.

Downloaded from <http://advances.sciencemag.org/> on June 18, 2020

of these maps shown in Fig. 4 (F to J) reflects the momentum structure of the quasiparticles at the corresponding energies. To quantitatively visualize the quasiparticle dispersions, we take linecuts of the energy-dependent FTs along the two high-symmetry directions (Fig. 5). In addition, the different QPI wave vectors observed in the raw FTs are fit to Gaussians at each energy, and the results are plotted as orange data points in Fig. 5 (see section S8). The maps reveal three heavy bands at  $E_1$ ,  $E_0$ , and  $E_2$  (the latter only partially observed) and their hybridization with strongly dispersive conduction electron bands. The hybridization is stronger along the  $[\pi/a, \pi/a]$  direction as compared with the  $[2\pi/a, 0]$  direction. Last, the effective mass of the electron  $m^*$  is extracted from the curvature  $\frac{1}{4}\hbar^2 \left[ \frac{d^2E}{dq^2} \right]^{-1}$  of a second-order polynomial fit (quadratic band structure) to the QPI bands crossing  $E_F$  (red lines in Fig. 5, A and B). Our findings of  $m^* = (8 \pm 2)m_0$  and  $(8 \pm 6)m_0$  along the  $(\pi/a, \pi/a)$  and  $(2\pi/a, 0)$  directions, respectively, are in good agreement with the results from the dHvA experiments (43).

## DISCUSSION

Our studies reveal two important findings in the context of heavy fermions. First, the gradual emergence of a sharp quasiparticle peak near the  $E_F$  ( $E_0$  resonance), its Kondo hole signature around Th dopants, and its hybridization with conduction electrons provide a comprehensive picture of the coherent Kondo lattice formation developing deep inside the AFM phase ( $T_{KL} \ll T_N$ ). This conclusion indicates

that, in  $\text{USb}_2$ , the coherent Kondo lattice does not break down on the AFM side of the heavy fermion phase diagram; rather, it emerges from within. The insensitivity of the AFM order to the formation of the Kondo lattice at  $T_{coh} \sim 80$  K in our neutron scattering experiment along with the orbital selectivity provided by the DMFT calculations together demonstrate the dual itinerant and localized nature of the  $f$  electrons residing on different  $f$  orbitals. This picture is different from, for example, the Kondo breakdown scenario observed in  $\text{YbRh}_2\text{Si}_2$ , where the Kondo lattice and AFM order are separated by a single QCP.

Second, the discovery of a pair of nontrivial sharp electronic bands, asymmetrically placed above and below the  $E_F$  at  $E_1$  and  $E_2$  emerging abruptly at 45 K, indicates a new form of electronic transition. The origin of these flat bands may be suggestive of orbital ordering, but the mechanism of their abrupt, most likely first order-like transition (note that no hint of  $E_{1,2}$  is observed at 52 K; Fig. 2A) is mysterious and calls for further investigations. Yet, it is tempting to make some speculations about possible connections to the “hidden-order” phase of  $\text{URu}_2\text{Si}_2$ , which itself is closely connected (first-order phase transition) to an AFM phase (44). In  $\text{URu}_2\text{Si}_2$ , a pair of quasiparticle bands of the U 5f electrons asymmetrically form very close (few millielectron volts) to the  $E_F$  (25, 45) and hybridize with conduction electrons in the hidden-order phase (21). Although the energy scales involved in the two U compounds are very different (by an order of magnitude), the overall resemblance with our observation here perhaps raises a possibility of some connection between the two material systems and calls for future investigations.

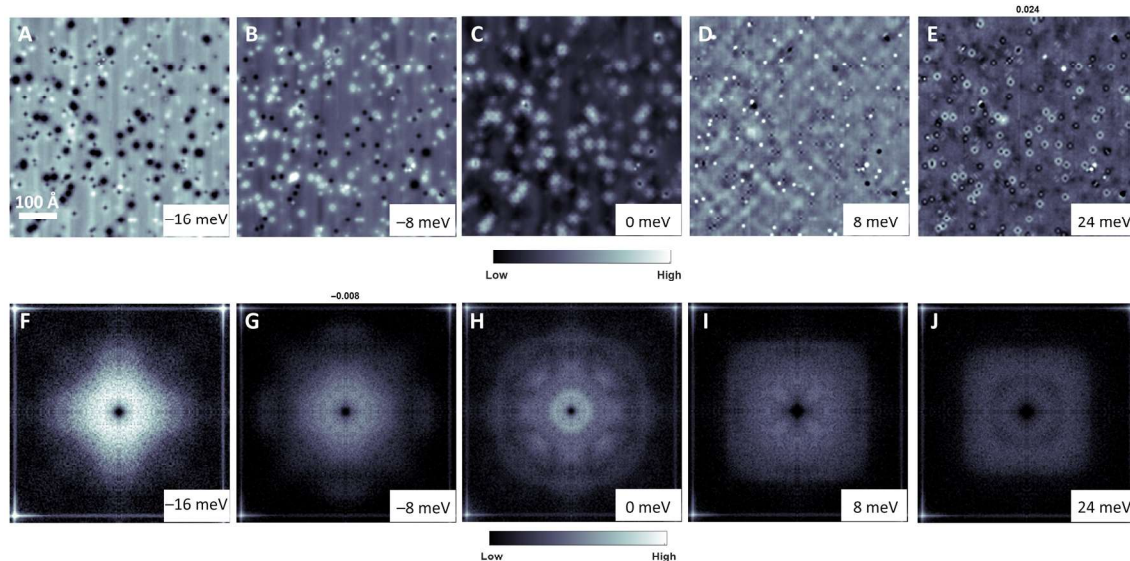


**Fig. 4. Spectroscopic imaging of the QPI.** (A to E) Real-space conductance maps ( $-400$  mV,  $-2$  nA) at selected energies for  $x = 0.3\%$  Th doping, showing strong QPI near the Th dopants. (F to J) FTs of the same maps revealing rapidly dispersive features of the QPI in the momentum space.

Downloaded from <http://advances.sciencemag.org/> on June 18, 2020

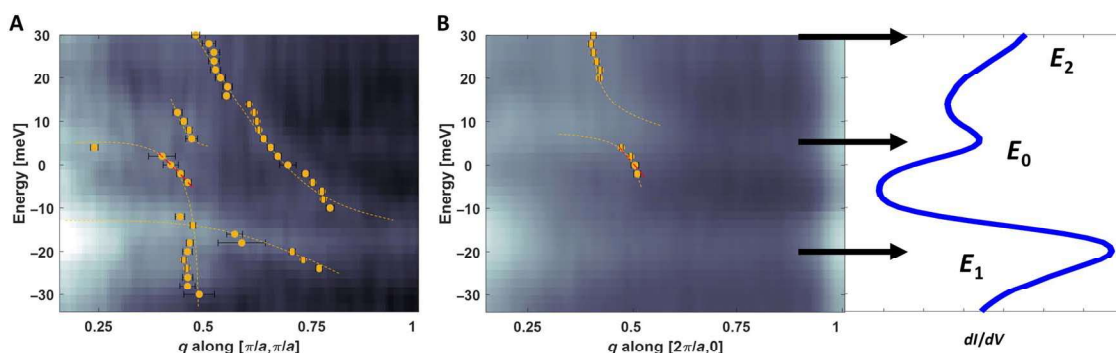


**Fig. 5. Visualizing energy-momentum structure of quasiparticles.** (A and B) Energy dispersion of the quasiparticles scattering along the  $(\pi/a, \pi/a)$  (A) and  $(2\pi/a, 0)$  (B) directions. Three bands corresponding to  $E_0$ ,  $E_1$ , and  $E_2$  appear to hybridize with conduction electrons. The data points are extracted from Gaussian fits to linecuts in the FT (see the Supplementary Materials). For the  $(2\pi/a, 0)$  direction, the dispersion at  $E_0$  is very rapid, making extraction of the precise wave vector meaningless. The dashed lines are a guide to the eye. The red lines are a quadratic fit to the data points that cross  $E_F$ . The effective mass is extracted from the curvature  $\frac{1}{4}\hbar^2 \left[ \frac{d^2E}{dq^2} \right]^{-1}$  of the second-order polynomial fit.

## MATERIALS AND METHODS

### Sample growth

Single crystals of  $U_{1-x}Th_xSb_2$  were grown out of an Sb flux using conventional high-temperature solution growth techniques. Small chunks of U, Th, and Sb were mixed together according to the ratio  $U:Th:Sb = 1 - x:x:11.5$ . Single crystals were grown by slowly cooling down the U-Th-Sb melt from  $1100^\circ$  to  $700^\circ$ C over 80 hours and then decanting off the excess liquid flux. Identification of commercial equipment does not imply recommendation or endorsement by the National Institute of Standards and Technology (NIST).

### Scanning tunneling microscopy

Flat samples of  $\sim(1 \times 1 \times 0.5)$  mm were glued to a metallic plate using an H74F epoxy, and a conducting channel to the plate was achieved using an H20E silver conducting epoxy. Identification of epoxy products does not imply recommendation or endorsement by the NIST. An aluminum post was attached to the exposed surface of the sample using an

H74F epoxy, oriented along the sample's (001) plane. The samples were cleaved in situ under ultra-high vacuum by knocking the post off, transferred immediately to the microscope head, and cooled down to  $\sim 8.5$  K. PtIr tips were used in all experiments, and prior to each experiment, the tips were prepared on the Cu(111) surface that has been treated to several cycles of sputtering with Ar and annealing before placed in the microscope head to cool. The sample and the Cu(111) were placed inside the microscope head next to each other to minimize exposure and preserve the structural integrity of the tip when moving between the two. STM topographies were taken at a constant current mode, and  $dI/dV$  measurements were performed using a lock-in amplifier with a reference frequency set at  $0.921$  kHz. The data presented in this paper were collected from six successfully cleaved samples equally distributed between the different Th percentage doping ( $x = 0$ ,  $x = 0.3\%$ , and  $x = 0.5\%$ ). There were negligible differences measured between different cleaves and different areas on a sample. The error bars correspond to uncertainty of 1 SD.

## Neutron diffraction

Neutron diffraction measurements were performed (on the same single crystals used in our STM experiments) at the BT-7 thermal triple axis spectrometer at the NIST Center for Neutron Research using a 14.7-meV energy and collimation: open - 25' - sample - 25' - 120'. The magnetic intensity at the (1,0,0.5) peak was compared to the nuclear intensity at the (1,0,1) peak, while the temperature dependence of the (1,1,0.5) peak was used to calculate an order parameter. An  $f^2$  magnetic form factor was assumed. The error bars correspond to uncertainty of 1 SD.

## Dynamical mean field theory

We used density functional theory (DFT) plus DMFT (46), as implemented in the full-potential linearized augmented plane-wave method (47, 48), to describe the correlation effect on 5f electrons. The correlated U 5f electrons were treated dynamically by the DMFT local self-energy, while all other delocalized spd electrons were treated on the DFT level. The vertex-corrected one-crossing approximation (46) was adopted as the impurity solver, in which full atomic interaction matrix was taken into account. The Coulomb's interaction  $U = 4.0$  eV and the Hund's coupling  $J = 0.57$  eV were used for the DFT + DMFT calculations.

## SUPPLEMENTARY MATERIALS

Supplementary material for this article is available at <http://advances.sciencemag.org/cgi/content/full/5/10/eaaw9061/DC1>

Section S1. Identifying the cleaving plane and Th dopants

Section S2.  $dI/dV$  on different Th concentrations and temperature dependence measurements on  $x = 0$  and 0.5%

Section S3. X-ray absorption spectroscopy

Section S4. DFT and DMFT of electronic states of  $\text{USb}_2$

Section S5.  $dI/dV$  spectra fitting to Fano line shape

Section S6. Spatial modulation of the Kondo hole

Section S7. Energy-momentum structure from QPI

Section S8. Extraction of the QPI features

Fig. S1. Cleaving plane and Th dopants.

Fig. S2. T dependence.

Fig. S3. X-ray absorption spectroscopy.

Fig. S4. Dynamical mean field theory.

Fig. S5.  $dI/dV$  Fano fit.

Fig. S6. Spatial modulation of the Kondo hole.

Fig. S7. Linecuts of  $q$  maps.

Fig. S8. Hybridized bands and density of states.

Fig. S9. FT of fit parameters.

Fig. S10. FT of conductance maps for  $x = 0.5\%$ .

Fig. S11. Raw-symmetrized data comparison.

Fig. S12. Linecuts across QPI features.

References (49, 50)

## REFERENCES AND NOTES

1. J. A. Mydosh, P. M. Oppeneer, Hidden order behaviour in  $\text{URu}_2\text{Si}_2$  (A critical review of the status of hidden order in 2014). *Philos. Mag.* **94**, 3642–3662 (2014).
2. O. Stockert, F. Steglich, Unconventional quantum criticality in heavy-fermion compounds. *Annu. Rev. Condens. Matter Phys.* **2**, 79–99 (2011).
3. F. Steglich, S. Wirth, Foundations of heavy-fermion superconductivity: Lattice Kondo effect and Mott physics. *Rep. Prog. Phys.* **79**, 084502 (2016).
4. S. S. Saxena, P. Agarwal, K. Ahilan, F. M. Grosche, R. K. W. Haselwimmer, M. J. Steiner, E. Pugh, I. R. Walker, S. R. Julian, P. Monthoux, G. G. Lonzarich, A. Huxley, I. Sheikin, D. Braithwaite, J. Flouquet, Superconductivity on the border of itinerant-electron ferromagnetism in  $\text{UGe}_2$ . *Nature* **406**, 587–592 (2000).
5. D. Aoki, A. Huxley, E. Ressouche, D. Braithwaite, J. Flouquet, J.-P. Brison, E. Lhotel, C. Paulsen, Coexistence of superconductivity and ferromagnetism in  $\text{URhGe}$ . *Nature* **413**, 613–616 (2001).
6. P. Coleman, in *Handbook of Magnetism and Advanced Magnetic Materials*, H. Kronmueller, S. Parkin, Eds. (John Wiley & Sons Ltd., Chichester, UK, 2007).
7. Q. Si, S. Rabello, K. Ingersent, J. L. Smith, Locally critical quantum phase transitions in strongly correlated metals. *Nature* **413**, 804–808 (2001).
8. P. Coleman, C. Pépin, Q. Si, R. Ramazashvili, How do Fermi liquids get heavy and die? *J. Phys. Condens. Matter* **13**, R723–R738 (2001).
9. J. A. Hertz, Quantum critical phenomena. *Phys. Rev. B* **14**, 1165–1184 (1976).
10. A. J. Millis, Effect of a nonzero temperature on quantum critical points in itinerant fermion systems. *Phys. Rev. B* **48**, 7183–7196 (1993).
11. W. Knafo, S. Raymond, P. Lejay, J. Flouquet, Antiferromagnetic criticality at a heavy-fermion quantum phase transition. *Nat. Phys.* **5**, 753–757 (2009).
12. S. Friedemann, T. Westerkamp, M. Brando, N. Oeschler, S. Wirth, P. Gegenwart, C. Krellner, C. Geibel, F. Steglich, Detaching the antiferromagnetic quantum critical point from the Fermi-surface reconstruction in  $\text{YbRh}_2\text{Si}_2$ . *Nat. Phys.* **5**, 465–469 (2009).
13. S. Paschen, S. Friedemann, S. Wirth, F. Steglich, S. Kirchner, Q. Si, Kondo destruction in heavy fermion quantum criticality and the photoemission spectrum of  $\text{YbRh}_2\text{Si}_2$ . *J. Magn. Magn. Mater.* **400**, 17–22 (2016).
14. J. Leciejewicz, R. Troć, A. Murasik, A. Zygmunt, Neutron diffraction study of antiferromagnetism in  $\text{USb}_2$  and  $\text{UBi}_2$ . *Phys. Stat. Solidi* **22**, 517–526 (1967).
15. T. Durakiewicz, P. Riseborough, J.-Q. Meng, Resolving the multi-gap electronic structure of  $\text{USb}_2$  with interband self-energy. *J. Electron Spectrosc. Relat. Phenomena* **194**, 23–26 (2014).
16. D. Aoki, P. Wiśniewski, K. Miyake, N. Watanabe, Y. Inada, R. Settai, E. Yamamoto, Y. Haga, Y. Onuki, Cylindrical Fermi surfaces formed by a flat magnetic Brillouin zone in uranium dipnictides. *Philos. Mag. B* **80**, 1517–1544 (2000).
17. R. Wawryk, Magnetic and transport properties of  $\text{UBi}_2$  and  $\text{USb}_2$  single crystals. *Philos. Mag.* **86**, 1775–1787 (2006).
18. R. L. Stillwell, I.-L. Liu, N. Harrison, M. Jaime, J. R. Jeffries, N. P. Butch, Tricritical point of the f-electron antiferromagnet  $\text{USb}_2$  driven by high magnetic fields. *Phys. Rev. B* **95**, 014414 (2017).
19. J. R. Jeffries, R. L. Stillwell, S. T. Weir, Y. K. Vohra, N. P. Butch, Emergent ferromagnetism and T-linear scattering in  $\text{USb}_2$  at high pressure. *Phys. Rev. B* **93**, 184406 (2016).
20. P. Aynajian, E. H. da Silva Neto, C. V. Parker, Y. Huang, A. Pasupathy, J. Mydosh, A. Yazdani, Visualizing the formation of the Kondo lattice and the hidden order in  $\text{URu}_2\text{Si}_2$ . *Proc. Natl. Acad. Sci. U.S.A.* **107**, 10383–10388 (2010).
21. A. R. Schmidt, M. H. Hamidian, P. Wahl, F. Meier, A. V. Balatsky, J. D. Garrett, T. J. Williams, G. M. Luke, J. C. Davis, Imaging the Fano lattice to ‘hidden order’ transition in  $\text{URu}_2\text{Si}_2$ . *Nature* **465**, 570–576 (2010).
22. P. Aynajian, E. H. da Silva Neto, A. Gynis, R. E. Baumbach, J. D. Thompson, Z. Fisk, E. D. Bauer, A. Yazdani, Visualizing heavy fermions emerging in a quantum critical Kondo lattice. *Nature* **486**, 201–206 (2012).
23. A. Maldonado, H. Suderow, S. Vieira, D. Aoki, J. Flouquet, Temperature dependent tunneling spectroscopy in the heavy fermion  $\text{CeRu}_2\text{Si}_2$  and in the antiferromagnet  $\text{CeRh}_2\text{Si}_2$ . *J. Phys. Condens. Matter* **24**, 475602 (2012).
24. S. Ernst, S. Kirchner, C. Krellner, C. Geibel, G. Zwicknagl, F. Steglich, S. Wirth, Emerging local Kondo screening and spatial coherence in the heavy-fermion metal  $\text{YbRh}_2\text{Si}_2$ . *Nature* **474**, 362–366 (2011).
25. P. Aynajian, E. H. da Silva Neto, B. Zhou, S. Misra, R. E. Baumbach, Z. Fisk, J. Mydosh, J. D. Thompson, E. D. Bauer, A. Yazdani, Visualizing heavy fermion formation and their unconventional superconductivity in f-electron materials. *J. Phys. Soc. Jpn.* **83**, 061008 (2014).
26. B. B. Zhou, S. Misra, E. H. da Silva Neto, P. Aynajian, R. E. Baumbach, J. D. Thompson, E. D. Bauer, A. Yazdani, Visualizing nodal heavy fermion superconductivity in  $\text{CeCoIn}_5$ . *Nat. Phys.* **9**, 474–479 (2013).
27. M. P. Allan, F. Massee, D. K. Morr, J. Van Dyke, A. W. Rost, A. P. Mackenzie, C. Petrovic, J. C. Davis, Imaging Cooper pairing of heavy fermions in  $\text{CeCoIn}_5$ . *Nat. Phys.* **9**, 468–473 (2013).
28. K. Momma, F. Izumi, VESTA 3 for three-dimensional visualization of crystal, volumetric and morphology data. *J. Appl. Cryst.* **44**, 1272–1276 (2011).
29. M. Maltseva, M. Dzero, P. Coleman, Electron cotunneling into a Kondo lattice. *Phys. Rev. Lett.* **103**, 206402 (2009).
30. J. Figgins, D. K. Morr, Differential conductance and quantum interference in Kondo systems. *Phys. Rev. Lett.* **104**, 187202 (2010).
31. P. Wölfe, Y. Dubi, A. V. Balatsky, Tunneling into clean heavy fermion compounds: Origin of the Fano line shape. *Phys. Rev. Lett.* **105**, 246401 (2010).
32. Z. Sun, A. Maldonado, W. S. Paz, D. S. Inosov, A. P. Schnyder, J. J. Palacios, N. Y. Shitsevalova, V. B. Filipov, P. Wahl, Observation of a well-defined hybridization gap and in-gap states on the  $\text{SmB}_6$  (001) surface. *Phys. Rev. B* **97**, 235107 (2018).
33. W. Ruan, C. Ye, M. Guo, F. Chen, X. Chen, G.-M. Zhang, Y. Wang, Emergence of a coherent in-gap state in the  $\text{SmB}_6$  Kondo insulator revealed by scanning tunneling spectroscopy. *Phys. Rev. Lett.* **112**, 136401 (2014).
34. S. Rößler, T.-H. Jang, D.-J. Kim, L. H. Tjeng, Z. Fisk, F. Steglich, S. Wirth, Hybridization gap and Fano resonance in  $\text{SmB}_6$ . *Proc. Natl. Acad. Sci. U.S.A.* **111**, 4798–4802 (2014).
35. J. Qi, T. Durakiewicz, S. A. Trugman, J.-X. Zhu, P. S. Riseborough, R. Baumbach, E. D. Bauer, K. Gofryk, J.-Q. Meng, J. J. Joyce, A. J. Taylor, R. P. Prasankumar, Measurement of two low-temperature energy gaps in the electronic structure of antiferromagnetic  $\text{USb}_2$  using ultrafast optical spectroscopy. *Phys. Rev. Lett.* **111**, 057402 (2013).

36. T. Durakiewicz, P. S. Riseborough, C. G. Olson, J. J. Joyce, P. M. Oppeneer, S. Elgazzar, E. D. Bauer, J. L. Sarrao, E. Guziewicz, D. P. Moore, M. T. Butterfield, K. S. Graham, Observation of a kink in the dispersion of  $f$ -electrons. *EPL Europhys. Lett.* **84**, 37003 (2008).
37. A. Yazdani, E. H. da Silva Neto, P. Aynajian, Spectroscopic imaging of strongly correlated electronic states. *Annu. Rev. Condens. Matter Phys.* **7**, 11–33 (2016).
38. J. Figgins, D. K. Morr, Defects in heavy-fermion materials: Unveiling strong correlations in real space. *Phys. Rev. Lett.* **107**, 066401 (2011).
39. J.-X. Zhu, J.-P. Julien, Y. Dubi, A. V. Balatsky, Local electronic structure and fano interference in tunneling into a Kondo hole system. *Phys. Rev. Lett.* **108**, 186401 (2012).
40. F. P. Toldin, J. Figgins, S. Kirchner, D. K. Morr, Disorder and quasiparticle interference in heavy-fermion materials. *Phys. Rev. B* **88**, 081101(R) (2013).
41. M. H. Hamidian, A. R. Schmidt, I. A. Firsov, M. P. Allan, P. Bradley, J. D. Garrett, T. J. Williams, G. M. Luke, Y. Dubi, A. V. Balatsky, J. C. Davis, How Kondo-holes create intense nanoscale heavy-fermion hybridization disorder. *Proc. Natl. Acad. Sci. U.S.A.* **108**, 18233–18237 (2011).
42. V. Madhavan, W. Chen, T. Jamneala, M. F. Crommie, N. S. Wingreen, Tunneling into a single magnetic atom: Spectroscopic evidence of the Kondo resonance. *Science* **280**, 567–569 (1998).
43. D. Aoki, P. Wiśniewski, K. Miyake, N. Watanabe, Y. Inada, R. Settai, E. Yamamoto, Y. Haga, Y. Ônuki, Crystal growth and cylindrical fermi surfaces of USb<sub>2</sub>. *J. Phys. Soc. Jpn.* **68**, 2182–2185 (1999).
44. E. Hassinger, D. Aoki, F. Bourdarot, G. Knebel, V. Taufour, S. Raymond, A. Villaume, J. Flouquet, Suppression of hidden order in URu<sub>2</sub>Si<sub>2</sub> under pressure and restoration in magnetic field. *J. Phys. Conf. Ser.* **251**, 012001 (2010).
45. H.-H. Kung, R. E. Baumbach, E. D. Bauer, V. K. Thorsmølle, W.-L. Zhang, K. Haule, J. A. Mydosh, G. Blumberg, Chirality density wave of the “hidden order” phase in URu<sub>2</sub>Si<sub>2</sub>. *Science* **347**, 1339–1342 (2015).
46. G. Kotliar, S. Y. Savrasov, K. Haule, V. S. Oudovenko, O. Parcollet, C. A. Marianetti, Electronic structure calculations with dynamical mean-field theory. *Rev. Mod. Phys.* **78**, 865–951 (2006).
47. K. Haule, C.-H. Yee, K. Kim, Dynamical mean-field theory within the full-potential methods: Electronic structure of CeIrIn<sub>5</sub>, CeCoIn<sub>5</sub>, and CeRhIn<sub>5</sub>. *Phys. Rev. B* **81**, 195107 (2010).
48. P. Blaha, K. Schwarz, G. K. H. Madsen, D. F. Kvasnicka, J. Luitz, *Wien2k, an Augmented Plane Wave Plus Local Orbitals Program for Calculating Crystal Properties* (Technische Universität Wien, Austria, 2001).
49. L. Miao, R. Basak, S. Ran, Y. Xu, E. Kotta, H. He, J. D. Denlinger, Y.-D. Chuang, Y. Zhao, Z. Xu, J. W. Lynn, J. R. Jeffries, S. R. Saha, I. Giannakis, P. Aynajian, C.-J. Kang, Y. Wang, G. Kotliar, N. P. Butch, L. A. Wray, High temperature singlet-based magnetism from Hund’s rule correlations. *Nat. Commun.* **10**, 644 (2019).
50. V. Aji, C. M. Varma, I. Vekhter, Kondo effect in an antiferromagnetic metal: Renormalization group analysis and a variational calculation. *Phys. Rev. B* **77**, 224426 (2008).

**Acknowledgments:** We thank P. Coleman, W.-C. Lee, C. Singh, and M. Lawler for the helpful discussions. **Funding:** Work at Binghamton University is supported by the NSF CAREER under award no. DMR-1654482. G.K. and C.-J.K. are supported by the DOE BES under grant no. DE-FG02-99ER45761. **Author contributions:** I.G., J.L., and M.K. performed the STM measurements. I.G. performed the STM data analysis. S.R., Y.Z., J.W.L., Z.X., and I.G. performed the neutron scattering measurements. C.-J.K. and G.K. performed the DFT + DMFT calculations. L.M. and L.A.W. carried out the x-ray absorption spectroscopy. S.R., S.R.S., and N.P.B. synthesized and characterized the materials. P.A. wrote the manuscript. All authors commented on the manuscript. **Competing interests:** The authors declare that they have no competing interests. **Data and materials availability:** All data needed to evaluate the conclusions in the paper are present in the paper and/or the Supplementary Materials. Additional data related to this paper may be requested from the authors.

Submitted 4 February 2019

Accepted 25 September 2019

Published 18 October 2019

10.1126/sciadv.aaw9061

**Citation:** I. Giannakis, J. Leshen, M. Kawai, S. Ran, C.-J. Kang, S. R. Saha, Y. Zhao, Z. Xu, J. W. Lynn, L. Miao, L. A. Wray, G. Kotliar, N. P. Butch, P. Aynajian, Orbital-selective Kondo lattice and enigmatic  $f$  electrons emerging from inside the antiferromagnetic phase of a heavy fermion. *Sci. Adv.* **5**, eaaw9061 (2019).

# Science Advances

## Orbital-selective Kondo lattice and enigmatic *f* electrons emerging from inside the antiferromagnetic phase of a heavy fermion

Ioannis Giannakis, Justin Leshen, Mariam Kavai, Sheng Ran, Chang-Jong Kang, Shanta R. Saha, Y. Zhao, Z. Xu, J. W. Lynn, Lin Miao, L. Andrew Wray, Gabriel Kotliar, Nicholas P. Butch and Pegor Aynajian

*Sci Adv* 5 (10), eaaw9061.  
DOI: 10.1126/sciadv.aaw9061

### ARTICLE TOOLS

<http://advances.sciencemag.org/content/5/10/eaaw9061>

### SUPPLEMENTARY MATERIALS

<http://advances.sciencemag.org/content/suppl/2019/10/10/5.10.eaaw9061.DC1>

### REFERENCES

This article cites 48 articles, 5 of which you can access for free  
<http://advances.sciencemag.org/content/5/10/eaaw9061#BIBL>

### PERMISSIONS

<http://www.sciencemag.org/help/reprints-and-permissions>

Use of this article is subject to the [Terms of Service](#)

---

Science Advances (ISSN 2375-2548) is published by the American Association for the Advancement of Science, 1200 New York Avenue NW, Washington, DC 20005. The title 'Science Advances' is a registered trademark of AAAS.

Copyright © 2019 The Authors, some rights reserved; exclusive licensee American Association for the Advancement of Science. No claim to original U.S. Government Works. Distributed under a Creative Commons Attribution NonCommercial License 4.0 (CC BY-NC).